Vacuum 201 (2022) 111064

Contents lists available at ScienceDirect

Vacuum

journal homepage: www.elsevier.com/locate/vacuum

# Solution-processed Y-doped $SnSrO_3$ electron transport layer for $Ga_2O_3$ based heterojunction solar-blind photodetector with high sensitivity

Chao Wu [a], Fengmin Wu [a,**], Lipeng Deng [a], Shan Li [b], Shunli Wang [a], Lin Cheng [a], Aiping Liu [a], Jinbin Wang [c], Weihua Tang [b,d], Daoyou Guo [a,*]

[a] Center for Optoelectronics Materials and Devices & Key Laboratory of Optical Field Manipulation of Zhejiang Province Department of Physics Zhejiang Sci-Tech University Hangzhou, 310018, China

[b] Laboratory of Information Functional Materials and Devices, School of Science, State Key Laboratory of Information Photonics and Optical Communications, Beijing University of Posts and Telecommunications, Beijing, 100876, China

[c] College of Materials Science and Engineering, Xiangtan University, Xiangtan, 411105, China

[d] College of Electronic and Optical Engineering & College of Microelectronics, National and Local Joint Engineering Laboratory for RF Integration and Micro-Packaging Technologies, Nanjing University of Posts and Telecommunications, Nanjing, 210046, China

A B S T R A C T

Since the transport behavior of carriers is crucial to the photodetection process, selecting a suitable electron transport layer (ETL) is an effective strategy for preparing high-performance photodetectors. However, developing high-efficiency and comprehensive bandgap ETL materials for deep UV photodetectors remains challenging. In this work, we used wide-bandgap $SrSnO_3$ nanoparticles to construct heterojunction solar-blind photodetectors with $Ga_2O_3$ by a simple solution-processing method. To improve carrier transportation efficiency, the $SrSnO_3$ was annealed in an oxygen atmosphere and doped with Y elements to reduce oxygen vacancies and increase conductivity. Compared to the untreated $SrSnO_3$, the oxygen vacancy of $SrSnO_3$ annealed under oxygen ($O_2$–$SrSnO_3$) decreased from 54.2% to 22.8%, while the conductivity of the Y doped $SrSnO_3$ (Y–$O_2$–$SrSnO_3$) increased about one order of magnitude. Thanks to this ETL engineering, the Y–$O_2$–$SrSnO_3$ exhibits the best carrier transportation efficiency, and the photodetector based on $\beta$-$Ga_2O_3$/Y–$O_2$–$SrSnO_3$ shows excellent photoelectrical performances with an $I_{on}/I_{off}$ ratio of $4.3 \times 10^6$, a detectivity of $1.3 \times 10^{13}$ Jones, and a solar-blind/visible ($R_{238\ nm}/R_{400\ nm}$) rejection ratio of $4.1 \times 10^3$. Our work provides a general strategy for building construct highly sensitive photodetectors, thus may push forward their applications.

## 1. Introduction

$Ga_2O_3$ based photodetectors attracted widespread attention and exhibited a broad application prospect in both the military and the civil fields due to their highly photosensitive and low false alarm rate [1–6]. Although several studies have been focused on photoconductive type $Ga_2O_3$ solar-blind photodetectors, which have simple device architecture and are easy to integrate, some disadvantages prevent them from being widely used, such as the slow response speed, the larger dark current, and the need for external power supply, etc. [7–15]. Photovoltaic type photodetectors (homojunction, heterojunction, and Schottky junction) utilize the junction effect to improve photodetection performance and can work without power well in line with the goals of developing low energy consumption devices. Although devices based on homojunction $Ga_2O_3$ p-n junction could exhibit satisfactory photodetection performance theoretically, p-type $Ga_2O_3$ have not been obtained due to the self-compensating effect. Given heterojunction type photodetectors have highly sensitive, fast response speeds and a simple preparation process, numerous $Ga_2O_3$ based heterojunction type photodetectors have been developed [16–29].

The working principle of heterojunction type photodetector includes two steps: (1) semiconductor material converts photons into electron-hole pairs when light irradiates with an energy greater than its bandgap. (2) The e-h pairs generated by the photons are divided by the barrier potential difference at the heterojunction, and then the electron transport to the electron-transport layer (ETL) while the holes migrate in the hole-transport layer (HTL) until the electrodes collect them. Several HTLs materials have been explored for use in $Ga_2O_3$ based heterojunction type photodetectors, including organic polymers (PEDOT: PSS, PTAA, Spiro-OMeTAD) and inorganic metal oxide (NiO, CuI, $CuGaO_2$), achieving excellent high self-powered performances [30–35]. However, the ETL materials have been rarely used in $Ga_2O_3$-based heterojunction photodetectors. Recently, inorganic perovskite oxides $SrSnO_3$ with easy synthesis pathways, high purity, good solubility, and stability have been

* Corresponding author.
** Corresponding author.
*E-mail addresses:* wfm@zstu.edu.cn (F. Wu), dyguo@zstu.edu.cn (D. Guo).

https://doi.org/10.1016/j.vacuum.2022.111064
Received 18 January 2022; Received in revised form 26 March 2022; Accepted 30 March 2022
Available online 5 April 2022

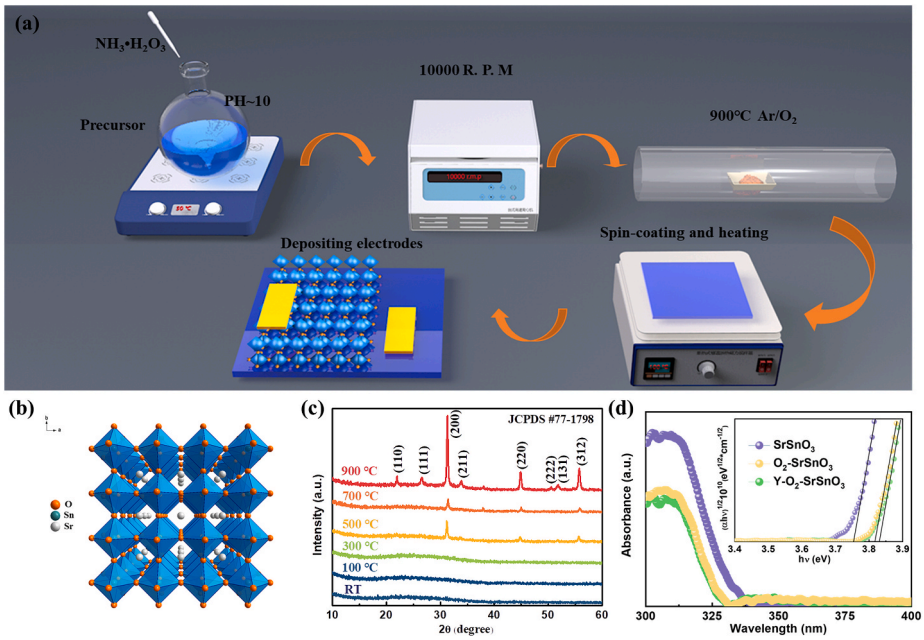


**Fig. 1.** (a) Schematic diagram of the preparation process of $SrSnO_3/Ga_2O_3$ heterojunction photodetectors. (b) Crystal structure of $SrSnO_3$. (c) XRD patterns of $SrSnO_3$ annealed at different temperatures. (d) UV–vis spectra of different $SrSnO_3$ nanoplates.

used as an ETL in various applications [36–40]. However, the lattice distortion due to the oxygen vacancies and the poor conductivity of the pristine $SrSnO_3$ make the charge carrier efficiency still unsatisfactory. Therefore, it is still highly desirable to optimize $SrSnO_3$ ETLs and improve their performance through electron transport engineering.

In this work, the solution-processed $SrSnO_3$ nanoparticles have been used to construct a type-II heterojunction solar-blind photodetector with $Ga_2O_3$ using a simple solution-processing method. For improving the carrier transportation efficiency of $SrSnO_3$, we annealed $SrSnO_3$ in an oxygen atmosphere and doped it with Y elements to reduce oxygen vacancies and increase conductivity, respectively. Notably, the $SrSnO_3$ doped with Y atoms and annealed under oxygen (Y–$O_2$–$SrSnO_3$) exhibit the best electron transportation efficiency, leading to better device performances. Thanks to this ETL engineering, the photodetector based on $\beta$-$Ga_2O_3$/Y–$O_2$–$SrSnO_3$ heterojunction shows excellent photoelectrical performances with an $I_{on}/I_{off}$ ratio of $4.3 \times 10^6$ and a detectivity of $1.3 \times 10^{13}$ Jones at 0 V. The high electron transport efficiency of Y–$O_2$–$SrSnO_3$ and the large built-in field in the $\beta$-$Ga_2O_3$/Y–$O_2$–$SrSnO_3$ heterojunction can be accountable for these outstanding performances. Our work provides a general strategy for building construct highly sensitive photodetectors, thus may push forward their applications.

## 2. Experimental section

### 2.1. Preparation and fabrication

$SrSnO_3$ and Y–$SrSnO_3$ nanoparticles were synthesized according to a slightly modified method from the previous literature [38–40]. $NH_3 \cdot H_2O$ was added into the precursor (0.01 M strontium chloride, 0.01 M Stannic chloride, and 0.005 M citric acid were dissolved in hydrogen peroxide solution for $SrSnO_3$. 0.0005 M Yttrium(III) nitrate hexahydrate, 0.0095 M strontium chloride, 0.01 M Stannic chloride, and 0.005 M citric acid was dissolved in hydrogen peroxide solution for Y–$SrSnO_3$) to adjust the pH value up to 10. The solution was then stirred at 50 °C for 60 min and centrifuged at 10,000 rpm as well as a wash with ethanol and deionized water to obtain $SrSnO_3$ nanoparticles. Finally, the as-grown nanoparticles were calcined at 100–900 °C in vacuum or $O_2$ to obtain a series of $SrSnO_3$ and Y–$SrSnO_3$ nanoparticles. To prepare the heterojunctions, $SrSnO_3$ and Y–$SrSnO_3$ nanoparticles were dispersed in 2-methoxy ethanol and spin-coated on the surface of $Ga_2O_3$. The 0.5 × 0.5 mm square Ti/Au metal were deposited onto the heterostructure as electrodes.

### 2.2. Characterization of materials and measurement of photoelectrical properties

The samples' crystal structure, component, and absorption spectrum were characterized by an X-ray diffractometer (D8), a spectrophotometer (U-3900 UV). X-ray photoelectron spectroscopy (XPS, Thermo Fisher-K-Alpha) was used to analyzed the chemical composition of the prepared $SrSnO_3$ nanoparticles. The XPS instrument kept the base pressure better than $3.5 \times 10^{-7}$ mTorr when used to acquire core-level XPS spectra from the sample. The spectrometer used Al Kα excitation source($h\nu = 1486.6$ eV), and the electron emission angle was 90°. The size of analyzed area was a circle of 500 μm in diameter. Samples were sputter-cleaned with an $Ar^+$ ion beam, where the $Ar^+$ incidence angle was about 50° with the $Ar^+$ energy of 1000 eV. The scanning speed is 1 eV/step. And the passing energy is 100 eV. Charge neutralizer was used. The binding energy was calibrated by the work function method. The samples' morphology was observed using a field-emission SEM (S4800, Hitachi) and a TEM (JEM-2100). The device's systematic photoelectric performances were tested by a Keithley 2400.

## 3. Results and discussion

The heterojunction's illustration appears in Fig. 1a, in which the $SrSnO_3$ nanoparticles were synthesized according to a slightly modified method from the previous works. In brief, the precursor solution is adjusted to a pH of 10 by adding ammonia and then stirred at 50 °C for 60 min. The solution was then centrifuged at 10,000 rpm and calcined at high temperatures to obtain $SrSnO_3$ nanoparticles. To construct $SrSnO_3/Ga_2O_3$ heterojunction photodetectors, the prepared $SrSnO_3$ nanoparticles were dispersed in 2-methoxy ethanol and spin-coated onto MOCVD-grown $Ga_2O_3$ at 3000 rpm followed by drying at 100 °C. $SrSnO_3$ has an orthorhombic $ABO_3$ perovskite structure (Fig. 1b), in which the oxygen atom occupies the vertices of the shared-angle octahedron BX6, while the metal Sn is located at the center of the octahedron and the metal Sr atom sited at the cavities of the 3D network [41–43]. The XRD

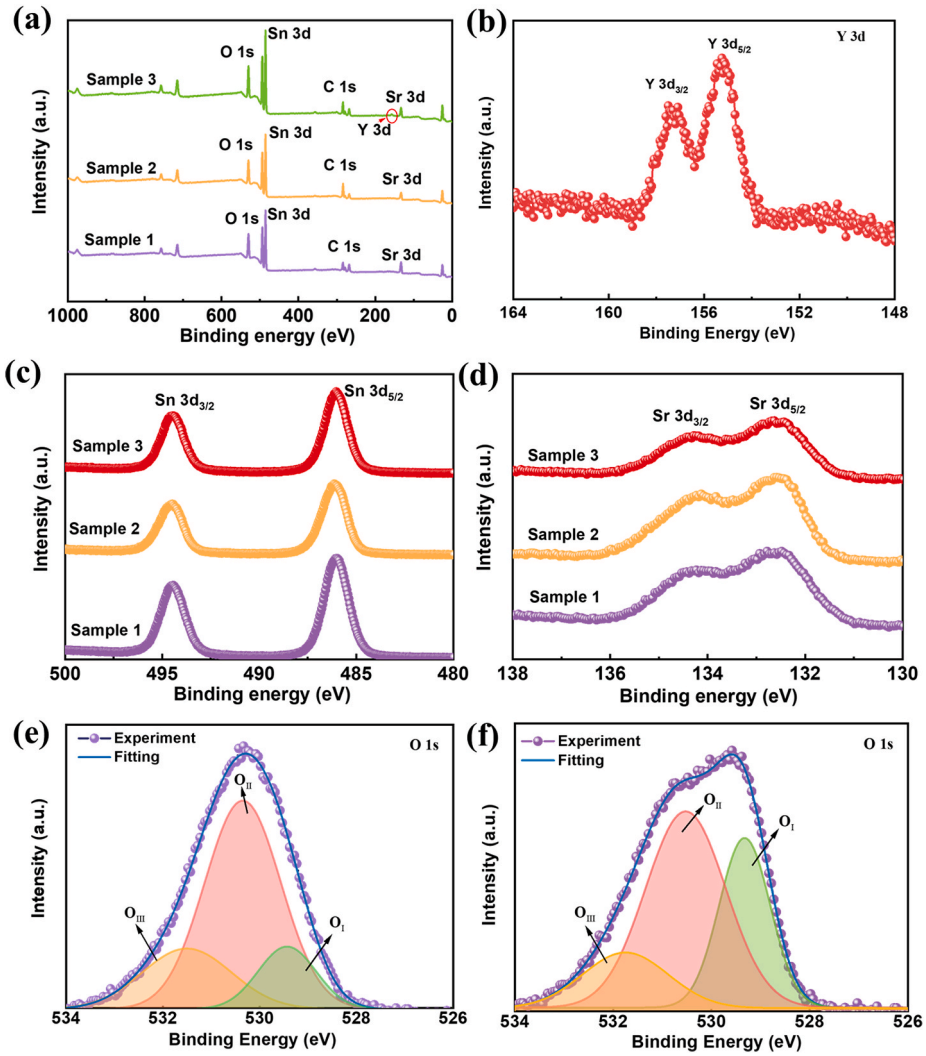


**Fig. 2.** (a) XPS patterns for all the samples. (b) Y 3d XPS patterns for Y doped $SrSnO_3$. (c) Sn 3d XPS patterns for all the samples. (d) Sr 3d XPS patterns for all the samples. (e) O 1s XPS patterns for $SrSnO_3$ annealed in vacuum. (f) O 1s XPS patterns for $SrSnO_3$ annealed in $O_2$.

results of $SrSnO_3$ calcined at the temperature ranging from 100 to 900 °C are shown in Fig. 1c, where the unannealed $SrSnO_3$ shows no obvious peaks indicating that it is amorphous. After annealing at 500 °C, a few weak diffraction peaks of $SrSnO_3$ appear, but the crystallization is still not ideal. Whereas, as the annealing temperature reached 900 °C, narrow diffraction peaks appeared at 21.9°, 26.5°, 30.7°, 44.7°, 50.3, 51.6 and 55.6° can be assigned to the (110), (111), (200) (211), (220), (222), (131) and (312) planes of orthorhombic $SrSnO_3$ (PDF#77–1798), respectively, indicating the excellent crystallization and high purity of the $SrSnO_3$ [44]. It is observed from the EDS results that the nanoplates contain Sr, Sn, and O elements, and the atomic percentage ratio is 22.06:19.27:58.67 (Sr: Sn:O), which is close to the atomic percentage ratio in $SrSnO_3$. The elemental maps of individual $SrSnO_3$ nanoplates indicated that the Sn, Sr, and O are distributed in the $SrSnO_3$ uniformly (Supporting information). The absorption edges of $SrSnO_3$ are 331 nm, while the absorption edges of $O_2$–$SrSnO_3$ and Y–$O_2$–$SrSnO_3$ are about

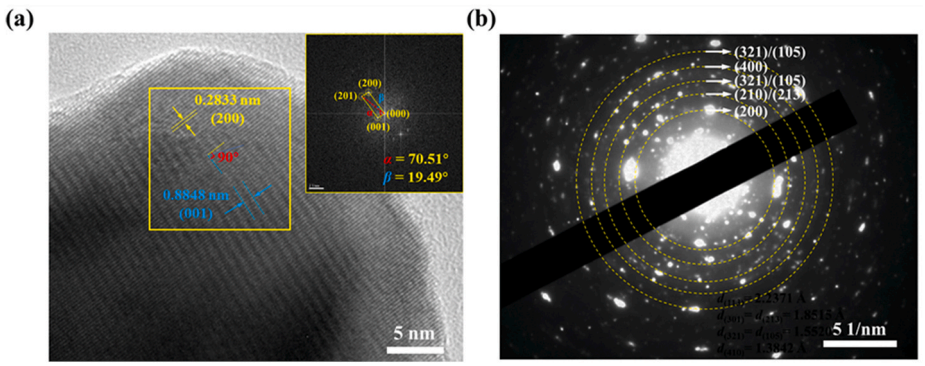


**Fig. 3.** (a) SAED pattern and (b) HRTEM image taken from the nanoplates shows high-quality crystallite.

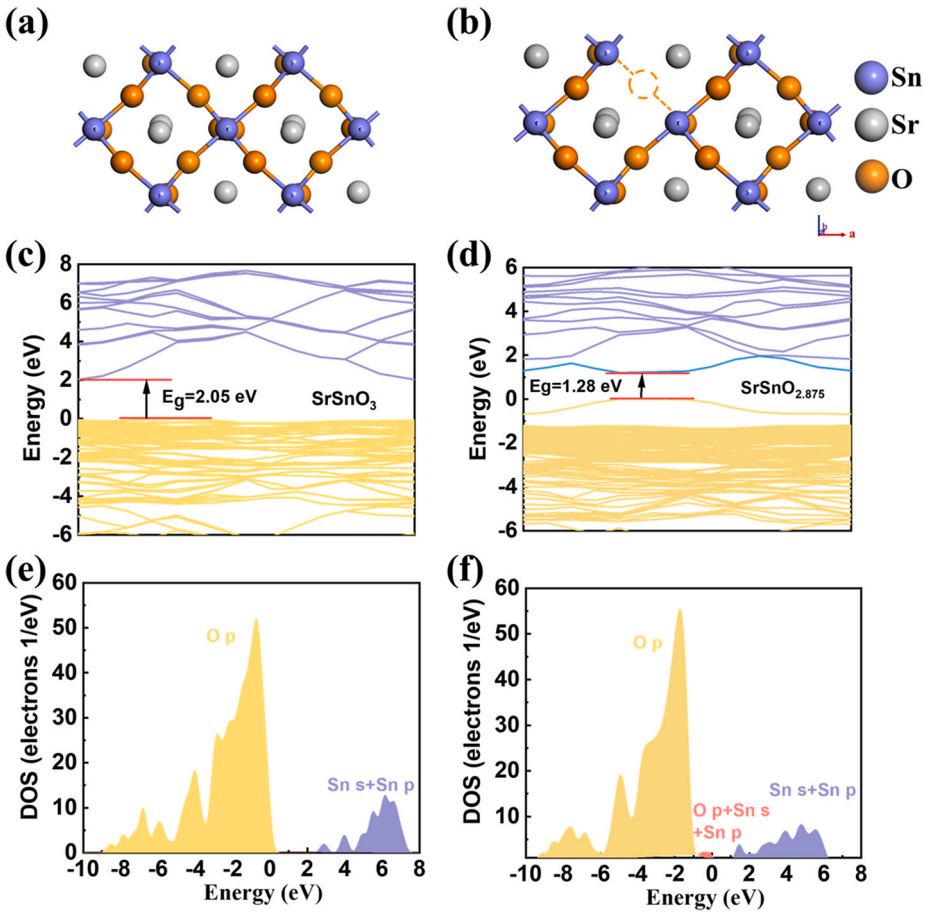


**Fig. 4.** (a) and (b) Atomic model of $SrSnO_3$ crystal structures with or without oxygen vacancy. (c) and (d) The calculations of the band structure of $SrSnO_3$ and $SrSnO_{2.875}$. (e) and (f) The calculations of the DOS of $SrSnO_3$ and $SrSnO_{2.875}$.

342 nm. These samples' band gaps ($E_g$) are inserted in Fig. 1d. The calculated band gap of $SrSnO_3$ increases from 3.75eV to 3.81eV as the oxygen vacancy decreases but remains almost constant with the doping of Y. X-ray photoelectron spectroscopies of all the $SrSnO_3$ samples are shown in Fig. 2. Greczynski et al. have demonstrated that the position of the C 1s peak of the adventitious carbon can vary from 284.08 to 286.74 eV. Therefore, the use of 284.8 eV as a charge reference for the C 1s peak of adventitious carbon is unreliable [45–48]. Fortunately, the sum of the binding energy of the C 1s with the work function of the sample ($\Phi_A$) is constant at 289.58 ± 0.14 eV, so calibration can be accomplished by setting the C 1s peak at 289.58-$\Phi_A$ eV. Considering that the work function of $SrSnO_3$ is 3.0 eV, the C 1s peak can be set at 286.58 eV. The peaks of the core levels Sr, Sn, and O have been observed, respectively (Fig. 2a). In addition, the characteristic peak of Y is detected in sample 3,

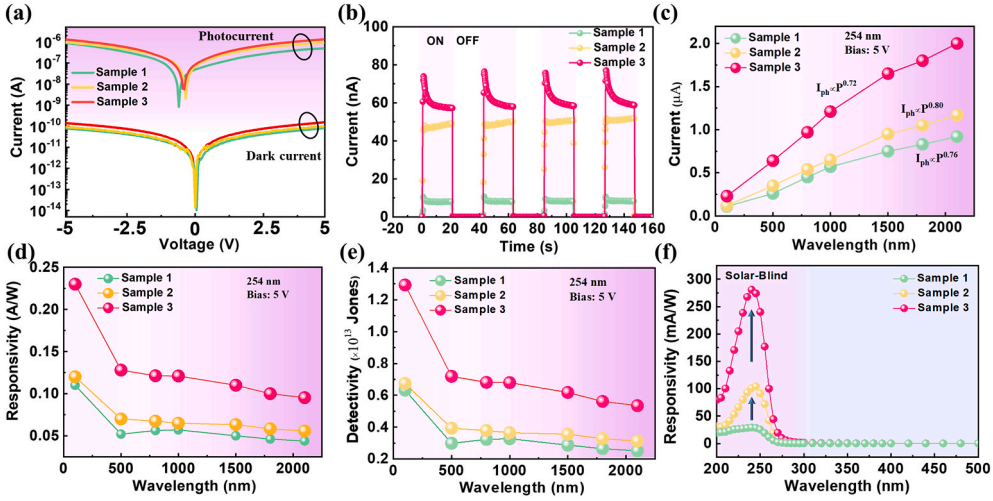


**Fig. 5.** (a) The typical *I–V* curves of sample 1 to sample 3. (b) Corresponding current-time (*I-t*) characteristics of sample 1 to sample 3. (c) Photocurrent of the photodetector under 254 nm light irradiation with various power intensities. (d) The responsivity of the photodetector under 254 nm light irradiation with various power intensities. (e) Detectivity of the photodetector under 254 nm light irradiation with various power intensities. (f) Spectral response of all the devices.

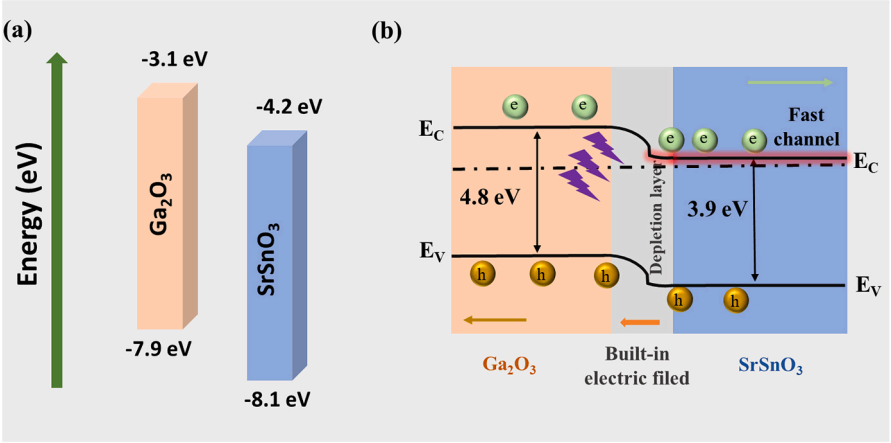


**Fig. 6.** (a) Energy band alignment diagrams and (b) Schematic diagram of charge carrier transfer on the $SrSnO_3/Ga_2O_3$ heterojunction.

further suggesting effective Y cations doping into the $SrSnO_3$ host lattice. The peaks of the Y 3d5/2 and Y 3d3/2 are located at 155.3 and 157.4 eV, respectively (Fig. 2b). The Sn 3d XPS spectra show two peaks at 486.0 and 494.5 eV, with a peak separation of 8.5 eV, which are attributed to Sr 3d5/2 and Sr 3d3/2 peaks respectively (Fig. 2c). The peaks of the Sr 3d5/2 and Sr 3d3/2 are located at 132.5 and 134.2 eV, respectively (Fig. 2d). There are no apparent changes for the Sr 3d and Sn 3d peaks for all samples. The XPS spectra of O 1s have three parent peaks as shown in Fig. 2e–f. One centered at 529.5 eV of all samples, which is related to lattice oxygen $O^{2-}$ ions in SSO lattice. Another one centered at 530.3 eV of three thin films, which is associated with $O^{2-}$ ions located at oxygen vacancy regions. The third one located at 531.6 eV is about O from adventitious carbon. Compared to the $SrSnO_3$ annealing under vacuum (Fig. 2e), the oxygen vacancy of $SrSnO_3$ annealed under oxygen (Fig. 2f) decreases. HRTEM images (Fig. 3) results prove that the $SrSnO_3$ NPs are highly crystalline with characteristic lattice plane of the (200) and (001) planes of the $SrSnO_3$, while the corresponding SAED pattern confirms their pure orthorhombic phase.

To investigate the mechanism of the effect of oxygen vacancy on the bandgap, a theoretical calculation on $SrSnO_3$ was carried out. Fig. 4a and b shows the atomic model of $SrSnO_3$ and $SrSnO_{2.875}$ crystal structures respectively. By optimizing the $SrSnO_3$ supercell, the bandgap of $SrSnO_3$ with $V_O$ is smaller than pure $SrSnO_3$, well in line with our experimental results. An impurity energy level between the CBM and the VBM (Fig. 4d) comes from the $V_O$ of $SrSnO_{2.875}$. As shown in the density of states (Fig. 4e and 4f), the $SrSnO_3$ valence band consists entirely of O 2p while the conduction band consists mainly of Sn 5s as well as Sn 5p orbitals. In contrast, the impurity energy level of $SrSnO_{2.75}$ consists of a mixture of O 2p, Sn 5s, and Sn 5p states. To further verify the electronic transmission efficiency of the $SrSnO_3$, steady-state photoluminescence was measured and shown in SFig. 2. The intensity of the PL peaks located at 763 nm of the $Ga_2O_3$/Y–$O_2$–$SrSnO_3$ is the lowest, indicating that Y–$O_2$–$SrSnO_3$ has the best carrier transportation efficiency. To investigate the impacts of the $SrSnO_3$ ETL on the photodetection performances, the Au/Ti–$SrSnO_3$/$Ga_2O_3$–Ti/Au heterojunction photodetectors are constructed.

The photodetector used $SrSnO_3$, $O_2$–$SrSnO_3$ and Y–$O_2$–$SrSnO_3$ were labeled as samples 1–3, respectively. Profited from the high-quality $Ga_2O_3$ films and the excellent heterojunction interface, all the photodetectors exhibit very small dark currents, only $10^{-14}$ at 0 V and a dozen sub-picoamps at −5 V (Fig. 5(a)). Higher electronic transportation efficiency is favorable for e-h pairs separation; therefore, the photocurrent of sample 3 under a 254 nm light is approximately tenfold higher than sample 1. The instantaneous *I-t* characteristics are displayed in Fig. 5b, from which sample 3 exhibits stable photoresponse with the largest on/off ratio of $4.3 \times 10^6$ among all the samples. The detailed photoelectricity relying on the power intensities in the range of 100–2100 μW/cm$^2$ are measurement and shown in Fig. 5c–f. The photocurrent of the device shows a non-linear variation as the light intensity, which is due to the more trap states being filled at higher power intensities. As the light power intensity changes from 100 to 2100 W/cm$^2$, both the responsivities ($R$) and detectives ($D$) decrease from high values to stable states [49,50]. Sample 3 exhibits the largest $R$ and $D$ values of about 23 mA/W and $1.29 \times 10^{13}$ joneses, respectively, under a 100 μW/cm$^2$ 254 nm light (Fig. 5d and 5e). The spectral responsivity curves of all the devices exhibit a narrow band centered at 238 nm attesting to their potential application in solar-blind photodetection. As expected, the spectral responsivity of sample 3 is much better than that of the other photodetectors, which exhibit highly spectrum selective with a solar-blind/UV ($R_{238}$ nm/$R_{280}$ nm) and solar-blind/visible ($R_{238}$ nm/$R_{400}$ nm) rejection ratio of about 576 and 4114, respectively. Comparisons between the our work and some previous reports are listed in Table S1 (supporting information). As self-powered solar-blind photodetectors, the $\beta$-$Ga_2O_3$/$SrSnO_3$ photodetectors show a lower dark current, a higher PDCR, and a faster response speed compared to some other photodetectors.

To better understand the reasons of the $SrSnO_3/Ga_2O_3$ photodetectors exhibit self-powered characteristics and excellent performance, the corresponding schematics of heterojunction energy bands and charge carrier transport are shown in Fig. 6. $SrSnO_3$ can form type-II staggered band alignment with $Ga_2O_3$. When they come into contact, the charge carriers diffuse and flow, leading the Fermi level line up and a band bending effect at the interface as well as creating a depletion layer. Y–$O_2$–$SrSnO_3$ with high electron transportation efficiency makes an expressway for electron transport and reduces the recombination process, improving photoelectric detection performance. The high electron transport efficiency of Y–$O_2$–$SrSnO_3$ and the large built-in field in the heterojunction can be accountable for these outstanding performances.

## 4. Conclusion

Herein, $SrSnO_3$ nanoparticles have been used as an electron transfer layer in $Ga_2O_3$ based photodetectors via a simple solution-processing method. The carrier transportation efficiency of the $SrSnO_3$ was improved by annealing in an oxygen atmosphere and doping with Y elements. The Y–$O_2$–$SrSnO_3$, with a high electrons transportation efficiency, makes an expressway for electrons transport and reduces the recombination process, improving better photoelectric detection performance. Thanks to this ETL engineering, the photodetector shows an excellent photoelectrical performance with an $I_{on}/I_{off}$ ratio of $4.3 \times 10^6$, a detectivity of $1.3 \times 10^{13}$ Jones, and a solar-blind/visible ($R_{238}$ nm/$R_{400}$ nm) rejection ratio of $4.1 \times 10^3$. This work provides a general strategy for building construct highly sensitive photodetectors, thus may push forward their applications.

## CRediT authorship contribution statement

**Chao Wu:** Writing – review & editing, Writing – original draft, Investigation, Conceptualization. **Fengmin Wu:** Resources, Project administration, Funding acquisition, Conceptualization. **Lipeng Deng:** Investigation, Formal analysis. **Shan Li:** Methodology, Investigation. **Shunli Wang:** Supervision, Resources. **Lin Cheng:** Supervision, Investigation. **Aiping Liu:** Supervision, Resources, Project administration. **Jinbin Wang:** Resources, Funding acquisition. **Weihua Tang:** Resources, Conceptualization. **Daoyou Guo:** Writing – review & editing, Supervision, Project administration, Funding acquisition.

## Declaration of competing interest

The authors declare that they have no known competing financial interests or personal relationships that could have appeared to influence the work reported in this paper.

## Acknowledgements

This work was supported by the National Natural Science Foundation of China (No. 61704153) and the fund of innovation center of radiation application (No. KFZC2021020403).

## Appendix A. Supplementary data

Supplementary data to this article can be found online at https://doi.org/10.1016/j.vacuum.2022.111064.

## References

[1] D. Kaur, M. Kumar, A strategic review on gallium oxide based deep-ultraviolet photodetectors: recent progress and future prospects, Adv. Opt. Mater. (2021), 2002160.
[2] X. Hou, Y. Zou, M. Ding, Y. Qin, Z. Zhang, X. Ma, P. Tan, S. Yu, X. Zhou, X. Zhao, G. Xu, H. Sun, S. Long, Review of polymorphous $Ga_2O_3$ materials and their solar-blind photodetector applications, J. Phys. D Appl. Phys. 54 (2021), 043001.
[3] Y. Qin, H.D. Sun, S.B. Long, G.S. Tompa, T. Salagaj, H. Dong, Q.M. He, G.Z. Jian, Q. Liu, H.B. Lv, M. Liu, High-performance metal-organic chemical vapor deposition grown ε-$Ga_2O_3$ solar-blind photodetector with asymmetric Schottky electrodes, IEEE Electron. Device Lett. 40 (2019) 1475.
[4] C. Wu, F.M. Wu, H.Z. Hu, C.Q. Ma, J.H. Ye, S.L. Wang, H.P. Wu, J.B. Wang, A. P. Liu, D.Y. Guo, Work function tunable laser induced graphene electrodes for Schottky type solar-blind photodetectors, Appl. Phys. Lett. 120 (2022), 101102.
[5] Y. Qin, L.H. Li, X.L. Zhao, G.S. Tompa, H. Dong, G.Z. Jian, Q.M. He, P.J. Tan, X. H. Hou, Z.F. Zhang, S.J. Yu, H.D. Sun, G.W. Xu, X.S. Miao, K.H. Xue, S.B. Long, M. Liu, Metal-semiconductor-metal ε-$Ga_2O_3$ solar-blind photodetectors with a record-high responsivity rejection ratio and their gain mechanism, ACS Photonics 7 (2020) 812–820.
[6] C. Wu, F.M. Wu, C.Q. Ma, S. Li, A.P. Liu, X. Yang, Y.C. Chen, J.B. Wang, D.Y. Guo, A general strategy to ultrasensitive $Ga_2O_3$ based self-powered solar-blind photodetectors, Mater. Today Phys. 23 (2022), 100643.
[7] Y.-C. Chen, Y.-J. Lu, C.-N. Lin, Y.-Z. Tian, C.-J. Gao, L. Dong, C.-X. Shan, Self-powered diamond/β-$Ga_2O_3$ photodetectors for solar-blind imaging, J. Mater. Chem. C 6 (2018) 5727–5732.
[8] Z. Li, Z. An, Y. Xu, Y. Cheng, Y.n. Cheng, D. Chen, Q. Feng, S. Xu, J. Zhang, C. Zhang, Y. Hao, Improving the production of high-performance solar-blind β-$Ga_2O_3$ photodetectors by controlling the growth pressure, J. Mater. Sci. 54 (2019) 10335–10345.
[9] R. Lin, W. Zheng, D. Zhang, Y. Li, F. Huang, Brushed crystallized ultrathin oxides: recrystallization and deep-ultraviolet imaging application, ACS Appl. Electron. Mater. 1 (2019) 2166–2173.
[10] S. Luan, L. Dong, X. Ma, R. Jia, The further investigation of n-doped β-$Ga_2O_3$ thin films with native defects for Schottky-barrier diode, J. Alloys Compd. 812 (2020), 152026.
[11] X.R. Chen, W. Mi, J.W. Wu, Z.C. Yang, K.L. Zhang, J.S. Zhao, C.B. Luan, Y.L. Wei, A solar-blind photodetector based on β-$Ga_2O_3$ film deposited on MgO (100) substrates by RF magnetron sputtering, Vacuum 180 (2020), 109632.
[12] Y. Miao, B. Liang, Y.Y. Tian, T.H. Xiong, S.J. Sun, C.L. Chen, Epitaxial growth of β-$Ga_2O_3$ nanowires from horizontal to obliquely upward evolution, Vacuum 192 (2021), 110444.
[13] W. Zheng, F. Huang, R. Zheng, H. Wu, Low-dimensional structure vacuum-ultraviolet-sensitive (λ < 200 nm) photodetector with fast-response speed based on high-quality AlN micro/nanowire, Adv. Mater. 27 (2015) 3921–3927.
[14] W. Zheng, R. Lin, J. Ran, Z. Zhang, X. Ji, F. Huang, Vacuum-ultraviolet photovoltaic detector, ACS Nano 12 (2018) 425–431.
[15] W. Zheng, L. Jia, F. Huang, Vacuum-ultraviolet photon detections, iScience 23 (2020), 101145.
[16] Z.M. Li, T. Jiao, J.Q. Yu, D.Q. Hu, Y.J. Lv, W.C. Li, X. Dong, B.L. Zhang, Y.T. Zhang, Z.H. Feng, G.X. Li, G.T. Du, Single crystalline β-$Ga_2O_3$ homoepitaxial films grown by MOCVD, Vacuum 178 (2020), 109440.
[17] X.R. Chen, W. Mi, M. Li, J.Z. Tang, J.S. Zhao, L.W. Zhou, X.C. Zhang, C.B. Luan, Optoelectronic artificial synapses based on β-$Ga_2O_3$ films by RF magnetron sputtering, Vacuum 192 (2021), 110422.
[18] L.X. Qian, Y. Wang, Z.H. Wu, T. Sheng, X.Z. Liu, β-$Ga_2O_3$ solar-blind deep-ultraviolet photodetector based on annealed sapphire substrate, Vacuum 140 (2017), 106e110.
[19] D. Zhang, Z. Du, M.H. Ma, W. Zheng, S.X. Liu, F. Huang, Enhanced performance of solar-blind ultraviolet photodetector based on Mg doped amorphous gallium oxide film, Vacuum 159 (2019) 204–208.
[20] Y.J. Ma, B.Y. Feng, X.D. Zhang, T.W. Chen, W.B. Tang, L. Zhang, T. He, X. Zhou, X. Wei, H.Q. Fu, K. Xu, S.N. Ding, B.S. Zhang, High-performance β-$Ga_2O_3$ solar-blind ultraviolet photodetectors epitaxially grown on (110) $TiO_2$ substrates by metalorganic chemical vapor deposition, Vacuum 191 (2021), 110402.
[21] J.W. Gu, Y. Shen, D.D. Wen, J. Huang, J.M. Lai, F. Gu, M. Cao, Li J. Wang, J. H. Min, Marked effects of Al-rich AlN transition layers on the performance of CdZnTe films for solar-blind photodetector, Vacuum 193 (2021), 110539.
[22] K.Y. Gu, Z.L. Zhang, K. Tang, J. Huang, Y. Shang, Y. Shen, M.Y. Liao, L.J. Wang, Effect of a seed layer on microstructure and electrical properties of $Ga_2O_3$ films on variously oriented Si substrates, Vacuum 195 (2022), 110671.
[23] X. Wang, Z. Liu, Y.S. Zhi, S. Li, Z.P. Wu, P.G. Li, W.H. Tang, Preliminary study for the effects of temperatures on optoelectrical properties of β-$Ga_2O_3$ thin films, Vacuum 166 (2019) 79–83.
[24] J. Yu, Z. Nie, L. Dong, L. Yuan, D. Li, Y. Huang, L. Zhang, Y. Zhang, R. Jia, Influence of annealing temperature on structure and photoelectrical performance of β-$Ga_2O_3$/4H-SiC heterojunction photodetectors, J. Alloys Compd. 798 (2019) 458–466.
[25] D. Zhang, W. Lin, S. Liu, Y. Zhu, R. Lin, W. Zheng, F. Huang, Ultra-robust deep-uv photovoltaic detector based on graphene/$(AlGa)_2O_3$/GaN with high-performance in temperature fluctuations, ACS Appl. Mater. Interfaces 11 (51) (2019) 48071–48078.
[26] D. Zhang, W. Zheng, R. Lin, Y. Li, F. Huang, Ultrahigh EQE (15%) solar-blind uv photovoltaic detector with organic-inorganic heterojunction via dual built-in fields enhanced photogenerated carrier separation efficiency mechanism, Adv. Funct. Mater. 29 (2019), 1900935.
[27] A.S. Pratiyush, S. Krishnamoorthy, S. Kumar, Z. Xia, R. Muralidharan, S. Rajan, D. N. Nath, Demonstration of zero bias responsivity in mbe grown β-$Ga_2O_3$ lateral deep-uv photodetector, Jpn. J. Appl. Phys. 57 (2018), 060313.
[28] J. Yu, M. Yu, Z. Wang, L. Yuan, Y. Huang, L. Zhang, Y. Zhang, R. Jia, Improved photoresponse performance of self-powered β-$Ga_2O_3$/NiO heterojunction uv photodetector by surface plasmonic effect of pt nanoparticles, IEEE Trans. Electron. Dev. 67 (2020) 3199–3204.
[29] R. Zhuo, D. Wu, Y. Wang, E. Wu, C. Jia, Z. Shi, T. Xu, Y. Tian, X. Li, A self-powered solar-blind photodetector based on a $MoS_2$/β-$Ga_2O_3$ heterojunction, J. Mater. Chem. C 6 (2018) 10982–10986.
[30] M.E. Ayhan, M. Shinde, B. Todankar, P. Desai, A.K. Ranade, M. Tanemura, G. Kalita, Ultraviolet radiation-induced photovoltaic action in γ-CuI/β-$Ga_2O_3$ heterojunction, Mater. Lett. 262 (2020), 127074.
[31] S. Li, D. Guo, P. Li, X. Wang, Y. Wang, Z. Yan, Z. Liu, Y. Zhi, Y. Huang, Z. Wu, W. Tang, Ultrasensitive, superhigh signal-to-noise ratio, self-powered solar blind photodetector based on n-$Ga_2O_3$/p-CuSCN core-shell microwire heterojunction, ACS Appl. Mater. Interfaces 11 (2019) 35105–35114.
[32] K.H. Li, N. Alfaraj, C.H. Kang, L. Braic, M.N. Hedhili, Z. Guo, T.K. Ng, B.S. Ooi, Deep-ultraviolet photodetection using single-crystalline β-$Ga_2O_3$/NiO heterojunctions, ACS Appl. Mater. Interfaces 11 (2019) 35095–35104.
[33] S. Li, Y. Zhi, C. Lu, C. Wu, Z. Yan, Z. Liu, J. Yang, X. Chu, D. Guo, P. Li, Z. Wu, W. Tang, Broadband ultraviolet self-powered photodetector constructed on exfoliated β-$Ga_2O_3$/CuI core-shell microwire heterojunction with superior reliability, J. Phys. Chem. Lett. 12 (2020) 447–453.
[34] S. Li, Z. Yan, Z. Liu, J. Chen, Y. Zhi, D. Guo, P. Li, Z. Wu, W. Tang, A self-powered solar-blind photodetector with large $V_{oc}$ enhancing performance based on the PEDOT:PSS/$Ga_2O_3$ organic–inorganic hybrid heterojunction, J. Mater. Chem. C 8 (2020) 1292–1300.
[35] Z. Yan, S. Li, Z. Liu, Y. Zhi, J. Dai, X. Sun, S. Sun, D. Guo, X. Wang, P. Li, Z. Wu, L. Li, W. Tang, High sensitivity and fast response self-powered solar-blind ultraviolet photodetector with a β-$Ga_2O_3$/spiro-MeOTAD p–n heterojunction, J. Mater. Chem. C 8 (2020) 4502–4509.
[36] J. Ahmed, C.K. Blakely, S.R. Bruno, V.V. Poltavets, Synthesis of $MSnO_3$ (M = Ba, Sr) nanoparticles by reverse micelle method and particle size distribution analysis by whole powder pattern modeling, Mater. Res. Bull. 47 (2012) 2282–2287.
[37] E. Baba, D. Kan, Y. Yamada, M. Haruta, H. Kurata, Y. Kanemitsu, Y. Shimakawa, Optical and transport properties of transparent conducting La-doped $SrSnO_3$ thin films, J. Phys. D Appl. Phys. 48 (2015), 455106.
[38] Q. Gao, H. Chen, K. Li, Q. Liu, Band gap engineering and room-temperature ferromagnetism by oxygen vacancies in $SrSnO_3$ epitaxial films, ACS Appl. Mater. Interfaces 10 (2018) 27503–27509.
[39] H. Guo, H. Chen, H. Zhang, X. Huang, J. Yang, B. Wang, Y. Li, L. Wang, X. Niu, Z. Wang, Low-temperature processed yttrium-doped $SrSnO_3$ perovskite electron transport layer for planar heterojunction perovskite solar cells with high efficiency, Nano Energy 59 (2019) 1–9.
[40] H. Guo, H. Zhang, J. Yang, W. Gong, H. Chen, H. Wang, X. Liu, F. Hao, X. Niu, Y. Zhao, Lanthanum-doped strontium stannate for efficient electron-transport

layers in planar perovskite solar cells, ACS Appl. Energy Mater. 3 (2020) 6889–6896.
[41] Y. Li, H. Zhang, B. Guo, M. Wei, Enhanced efficiency dye-sensitized $SrSnO_3$ solar cells prepared using chemical bath deposition, Electrochim. Acta 70 (2012) 313–317.
[42] H. Mizoguchi, N.S. Bhuvanesh, Y.I. Kim, S. Ohara, P.M. Woodward, Hydrothermal crystal growth and structure determination of double hydroxides $LiSb(OH)_6$, $BaSn(OH)_6$, and $SrSn(OH)_6$, Inorg. Chem. 53 (2014) 10570–10577.
[43] K.P. Ong, X. Fan, A. Subedi, M.B. Sullivan, D.J. Singh, Transparent conducting properties of $SrSnO_3$ and $ZnSnO_3$, Apl. Mater. 3 (2015), 062505.
[44] T. Alammar, I. Hamm, V. Grasmik, M. Wark, A.V. Mudring, Microwave-Assisted Synthesis of Perovskite $SrSnO_3$ nanocrystals in ionic liquids for photocatalytic applications, Inorg. Chem. 56 (2017) 6920–6932.
[45] G. Greczynski, L. Hultman, Towards reliable X-ray photoelectron spectroscopy: sputter-damage effects in transition metal borides, carbides, nitrides, and oxides, Appl. Surf. Sci. 542 (2021), 148599.
[46] G. Greczynski, L. Hultman, Compromising science by ignorant instrument calibration-need to revisit half a century of published XPS data, Angew. Chem. Int. Ed. 59 (2020) 5002–5006.
[47] G. Greczynski, L. Hultman, X-ray photoelectron spectroscopy: towards reliable binding energy referencing, Prog. Mater. Sci. 107 (2020), 100591.
[48] G. Greczynski, L. Hultman, Reliable determination of chemical state in x-ray photoelectron spectroscopy based on sample-work-function referencing to adventitious carbon: resolving the myth of apparent constant binding energy of the C 1s peak, Appl. Surf. Sci. 451 (2018) 99–103.
[49] B. Zhao, F. Wang, H. Chen, L. Zheng, L. Su, D. Zhao, X. Fang, An ultrahigh responsivity (9.7 mA $W^{-1}$) self-powered solar-blind photodetector based on individual ZnO-$Ga_2O_3$ heterostructures, Adv. Funct. Mater. 27 (2017), 1700264.
[50] P. Li, H. Shi, K. Chen, D. Guo, W. Cui, Y. Zhi, S. Wang, Z. Wu, Z. Chen, W. Tang, Construction of GaN/$Ga_2O_3$ p-n Junction for an extremely high responsivity self-powered uv photodetector, J. Mater. Chem. C 5 (2017) 10562–10570.